IEEE AP-S Antennas and Propagation Society | IEEE Journal of Selected Topics in Electromagnetics, Antennas and Propagation

Received 12 December 2025; revised 5 June 2026; accepted 24 June 2026. Date of publication 1 July 2026; date of current version 13 July 2026.

Digital Object Identifier 10.1109/JSTEAP.2026.3709266

AI-Enabled Pixel-Metamaterial Butler Matrix With Extreme Aspect Ratio for Mobile U6G Multibeam Antenna Applications

MINGZHE HU [1,2] (GRADUATE STUDENT MEMBER, IEEE), PENGYU FU [1,2] (MEMBER, IEEE), YONGJIAN ZHANG [3] (MEMBER, IEEE), AND YUE LI [1,2,4] (SENIOR MEMBER, IEEE)

[1]Department of Electronic Engineering, Tsinghua University, Beijing 100084, China
[2]Beijing National Research Center for Information Science and Technology, Tsinghua University, Beijing 100084, China
[3]Unmanned System Research Institute, Northwestern Polytechnical University, Xi'an 710072, China
[4]State Key Laboratory of Space Network and Communications, Tsinghua University, Beijing 10084, China

CORRESPONDING AUTHOR: Yue Li (e-mail: lyee@tsinghua.edu.cn).

This work was supported in part by the National Natural Science Foundation of China under Grant U22B2016; in part by the National Key Research and Development Program of China under Grant 2021YFA0716601; and in part by China National Postdoctoral Program for Innovative Talents under Grant BX20250350.

(Invited Article)

ABSTRACT This article presents an ultracompact Butler matrix (BM) with an extreme aspect ratio for mobile phones. To overcome the stringent space constraints, we leverage pixel metamaterials optimized by the nondominated sorting genetic algorithm II (NSGA-II) to construct miniaturized 3-dB hybrid couplers. Four such couplers are arranged in a parallel configuration to minimize the aspect ratio, thereby facilitating integration with flexible printed circuits (FPCs) in mobile phones. Moreover, the couplers and their layout are elaborately co-designed to satisfy the precise phase relations required for beamforming in the BM. With an ultracompact footprint of 48.5 × 9 mm (1.1 λ_0 × 0.2 λ_0, where λ_0 is the free-space wavelength at the center frequency), the proposed BM achieves a 16% operating bandwidth, fully covering the upper 6 GHz (U6G) band. Integration of the BM with four bezel-mounted dipole antennas validates the design, generating four beams steered at $\pm 20^\circ$ and $\pm 65^\circ$. Measured results indicate that the efficiencies for four ports all exceed 50% across the U6G band. This work provides a compact and low-cost beamforming solution for mobile phones, demonstrating significant potential for future U6G applications.

INDEX TERMS AI, Butler matrix (BM), mobile antennas, multibeam antennas, nondominated sorting genetic algorithm II (NSGA-II), pixel metamaterials, upper 6 GHz (U6G).

INTRODUCTION

The upper 6 GHz band (U6G, 6.425–7.125 GHz) was officially designated by 3GPP in 2022 as a pivotal spectrum for 5G-Advanced and 6G networks. Positioned between the 5G sub-6 GHz and millimeter-wave (mmW) bands, the U6G band offers substantial advantages over lower frequency bands, including increased channel capacity and higher data rates, attributed to its wider bandwidth. Moreover, its coverage extends significantly beyond that of the mmW band. Recent studies have investigated U6G channel characteristics, analyzing both its potential and associated challenges [1], [2], [3], [4]. A primary challenge is supporting the same cell coverage in the U6G band under current co-site configuration constraints, i.e., without requiring denser base station deployment. Specifically, an additional 6 dB path loss at U6G frequencies compared with 3.5 GHz is reported in [1]. Reference [2] emphasizes that bridging the coverage gap in co-site scenarios demands advancements in both base stations and user equipment, i.e., mobile phones. For base stations, the use of larger-scale antenna arrays is a straightforward and crucial solution, while mobile phones require beamforming technology to compensate for the path loss. As calculated in [3], merely increasing the number of isotropic antennas on the user side is insufficient in rich propagation environments due to theoretical limits. Consequently, pattern-reconfigurable antenna arrays capable of generating multiple steerable beams are selected to enhance both uplink and downlink coverage. Although several studies have emerged on base station antenna design for the U6G band [5], [6], [7], [8], research on the mobile phone side remains lacking. Therefore, there is still an urgent need and a significant challenge of mobile antenna design in the U6G band.

Compared with the phased arrays with expensive transmitters and receivers, multibeam antenna arrays with passive feeding networks offer a more competitive solution for mobile U6G applications, due to their low cost and effective beamforming capability [9], [10], [11], [12], [13], [14]. Among these, the Butler matrix (BM) [15] is a typical beamforming network extensively studied to achieve multibeam radiation [16], [17], [18], [19], [20], [21], [22], [23], [24], [25], [26]. Despite exploring various miniaturization techniques, these designs still remain prohibitively large for seamless integration into space-limited environments like mobile phones [27], [28], [29]. Notably, for such applications, reducing the BM's length is far more crucial than its width. The width of the antenna array is usually fixed at over one wavelength. As such, the BM does not require significant compression in its width. A moderate width can match the antennas better, enabling short connections between the BM outputs and antenna feeds. Conversely, the BM's length is strictly limited by the available area of the flexible printed circuit (FPC), which is positioned above the battery and connects the upper and lower mainboards. Minimizing the length can effectively free up valuable space for other functional circuits. Therefore, achieving an extremely small length-to-width aspect ratio is not only a geometric miniaturization outcome, but also an important requirement for practical mobile integration. In [18], a substrate-integrated waveguide is employed to construct a BM with a length of 3.7 λ, due to the inherently long crossover structure. A miniaturized alternative is proposed in [19], but it only reduces the width, neglecting its overall length. Although it reaches a subwavelength width, additional space is still required for antenna integration. Besides, multilayer techniques are also explored. In [20] and [21], two-layer substrates are used for area reduction. In addition, a multifolded structure is proposed in [22], which successfully reduces the length to only 0.5 λ. However, it comes at the high expense of complexity and thickness, which contradicts the primary low-cost advantage of passive multibeam antennas. Considering the above works, the bottleneck of further miniaturization and pursuit of an extreme aspect ratio lies in its complex structure and stringent phase requirements. As a result, despite the advancements in prior works, existing designs cannot be readily applied to the extremely limited space in mobile phones.

Fortunately, beyond traditional design approaches, pixel metamaterials with AI-driven optimization techniques have attracted attention in the miniaturization of microwave circuits [30], [31], [32], [33], [34]. In [30], the concept of pixel metamaterials is introduced to BM design through pixelated patches and optimization of the potential links between them. Moreover, by applying genetic algorithm (GA), reference [31] successfully integrates an arbitrary phase shifter into the pixel metamaterial coupler, achieving a subwavelength 8 × 8 BM. Such advancement reveals the potential of a more compact and flexible topology, inspiring our work in this article. Besides, the effectiveness and superiority of AI-enabled pixel metamaterial design have been further validated by applications to the field of antenna design and optimization [35], [36], [37]. More broadly, AI-driven metamaterial design has been recognized as an important route for forward prediction, inverse design, and spectral correlation in electromagnetic structures [38].

In this article, we apply pixel metamaterials to both the topological design and miniaturization of the BM for U6G applications. Different from the previous work [31] relying on single-objective GA, we adopt the well-established multiobjective nondominated sorting genetic algorithm II (NSGA-II) to achieve a more balanced optimization of both amplitude and phase properties. Based on this algorithm, we propose an ultracompact BM with an extreme aspect ratio, which shows excellent beam-steering performance comparable to traditional ones with a much larger size. To further validate its practicality for mobile applications, a four-element antenna array is integrated with the proposed BM, and its multibeam radiation properties are measured. This work provides a promising, low-cost, and competitive solution for multibeam antenna design in mobile phones for U6G applications, effectively bridging the gap between base stations and user equipment.

MINIATURIZATION PRINCIPLE

Fig. 1 illustrates the application scenario of the multibeam system in mobile phones. The system comprises a four-element bezel-mounted antenna array, a compact feeding network embedded in the FPC, and signal inputs from the mainboard. Each input port excites a distinct radiation beam steered toward a specific direction. Due to the space constraints in mobile phones, the primary challenge is the design of an ultracompact feeding network that maintains beam-steering performance and achieves an extreme aspect ratio. This section provides a comprehensive analysis of the miniaturization principles applied to the feeding network.

Novel Topological Design

As shown in Fig. 2(a), a conventional 4 × 4 BM consists of four hybrid couplers, providing equal amplitude and a 90° phase difference between two output ports, two −45° phase shifters, and two crossovers. Such standard configurations make the length of the BM usually over one wavelength, which is infeasible for integration into the FPC. Besides, when considering the connection between the BM and the antenna array, four transmission lines with an identical phase are necessary. To address these two critical issues, we propose a novel topological design for an ultracompact and highly integrated BM, as depicted in Fig. 2(b). In this design, pixel-metamaterial couplers are employed to replace the traditional hybrid couplers, which offers two key

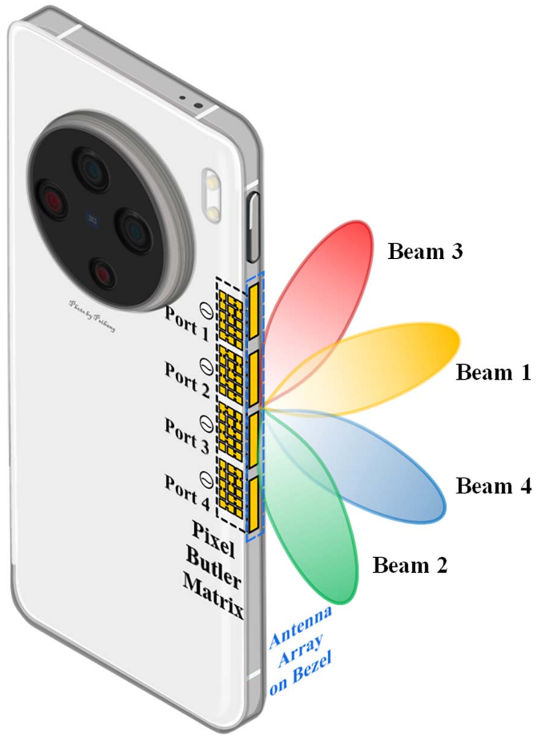

FIG. 1. Application scenario for the multibeam system in mobile phones. Each input port corresponds to a steered beam, with the feeding network on the flexible printed circuit and the antenna array on the bezel.

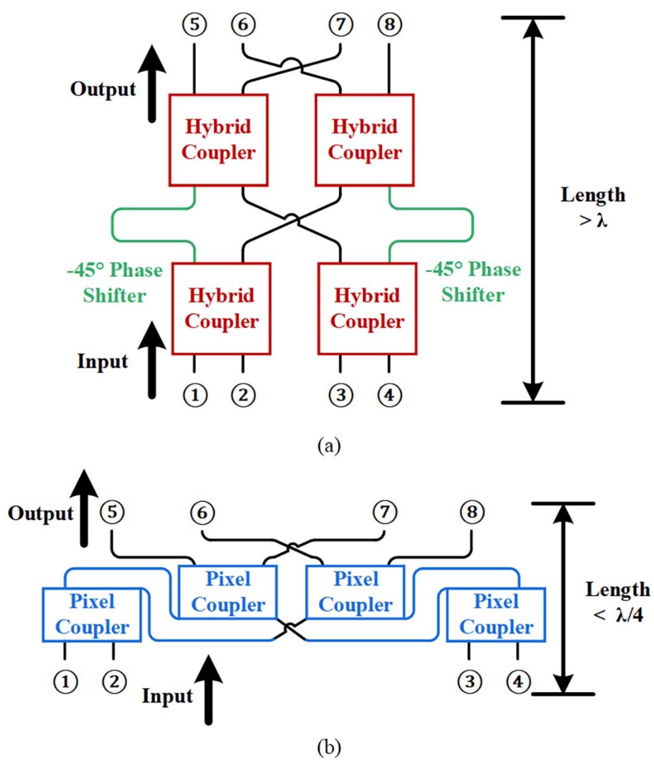

FIG. 2. (a) Conventional and (b) proposed novel topology of the Butler matrix.

advantages for miniaturization. First, due to a more efficient use of the available area, the size of each individual coupler can be reduced. Second, previous work [31] has presented the integration of phase shifters within the couplers, allowing for more flexible topology designs of the four couplers. Consequently, these couplers can be arranged in a compact, parallel configuration, as shown in Fig. 2(b). Through co-design with the connecting transmission lines, the specific phase requirements of this topology can be jointly optimized within the pixel metamaterial design. By combining these advantages, we achieve a highly compact BM topology with an extreme aspect ratio, making it suitable for integration in mobile phones.

AI-Enabled Pixel Metamaterials

To replace the traditional hybrid couplers in the proposed topology, we employ pixel metamaterials combined with AI-driven optimization technique. The fundamental pixel structure, the optimization procedures, and the flowchart of the NSGA-II algorithm are outlined in Fig. 3. The pixel metamaterial consists of a 2-D array of metallic patches, with potential connecting strips between adjacent patches. The freedom of design is maximized by modeling each strip as an inner port and controlling its state. By adjusting the port impedance to either zero or infinity, we can effectively simulate the physical presence or absence of the strip. Specifically, setting the impedance to zero ($Z_{ipn} = 0$) shorts the two adjacent patches by the strip, forming inductive coupling. Conversely, setting the impedance to infinity ($Z_{ipn} = \infty$) removes the strip, and the coupling becomes capacitive. Therefore, the states of all inner ports can be encoded as a binary sequence, where each unique sequence defines a specific physical layout and its corresponding electromagnetic properties.

The optimization process follows a three-step procedure. First, a full-wave pre-simulation is conducted, where all N inner ports and the four main ports are considered. This simulation yields the impedance matrix Z_{pre} of the entire $(N + 4)$-port network, as shown in (1). This matrix serves as the foundation for subsequent optimization

$$Z_{pre} = \begin{bmatrix} Z_{mp,mp} & Z_{mp,ip} \\ Z_{ip,mp} & Z_{ip,ip} \end{bmatrix}. \tag{1}$$

Here each element in the matrix is a matrix too. For example, $Z_{mp,mp}$ refers to the 4×4 impedance matrix of the four main ports. Similarly, $Z_{mp,ip}$ is the $4 \times N$ matrix of the mutual impedance between 4 main ports and N inner ports.

Second, for any given binary sequence defining the states of the N inner ports, we can construct an N-dimensional impedance matrix Z_{ip}, whose diagonal elements are either 0 or ∞ (a sufficiently large number for realization). The impedance matrix of the four main ports Z_{mp} corresponding to that specific binary sequence can be derived from the pre-simulation impedance matrix Z_{pre} of the $N + 4$ ports and the vector Z_{ip}. This is achieved by solving the set of equations (1)–(4), resulting in a closed-form expression of Z_{mp} given in (5)

$$\begin{bmatrix} V_{mp} \\ V_{ip} \end{bmatrix} = Z_{pre} \begin{bmatrix} I_{mp} \\ I_{ip} \end{bmatrix} \tag{2}$$

$$V_{ip} = Z_{ip} I_{ip} \tag{3}$$

$$V_{mp} = Z_{mp} I_{mp} \tag{4}$$

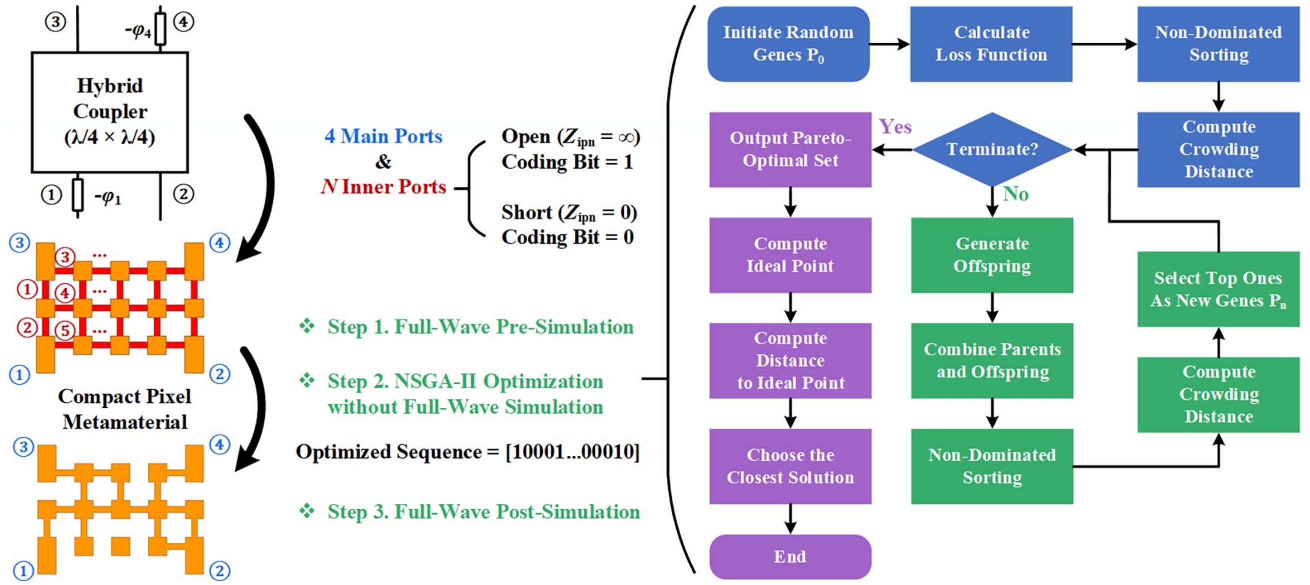

FIG. 3. Fundamental structures, optimization procedures, and flow chart of the algorithm of the pixel metamaterials.

$$Z_{\mathrm{mp}} = Z_{\mathrm{mp,mp}} + Z_{\mathrm{mp,ip}}(Z_{\mathrm{ip}} - Z_{\mathrm{ip,ip}})^{-1} Z_{\mathrm{ip,mp}}. \tag{5}$$

Subsequently, the S-parameters of the four-port coupler can be calculated from Z_{mp} using the impedance-to-scattering transformation, as shown in (6), where Z_0 is a diagonal matrix containing the normalization impedance

$$S_{\mathrm{mp}} = (Z_{\mathrm{mp}} - Z_0)(Z_{\mathrm{mp}} + Z_0)^{-1}. \tag{6}$$

Based on (6), a loss function can be calculated to quantify the deviation of the achieved S-parameters from the required ones, which provides the goal of optimization.

Third, once the algorithm converges on an optimal binary sequence, it is mapped back to a physical geometry of the strips. A final full-wave postsimulation is then performed to rigorously validate the performance optimized by the algorithm.

Different from traditional optimization based on full-wave simulations, the proposed method only requires two full-wave simulations by means of inner-port modeling and matrix calculation, achieving significant acceleration and enabling the application of advanced AI-driven optimization. Given the discrete, binary nature of the coding sequence, GA-based algorithm is preferred for optimization [31], [39], [40], [41], [42]. While prior work [31] employed a single-objective GA, we introduce a multiobjective formulation to achieve more balanced performance. The loss function is decomposed into a 3-D vector as shown in the following equation:

$$L_{\mathrm{total}} = [L_{\mathrm{amp-r}},\ L_{\mathrm{amp-t}},\ L_{\mathrm{phadif-t}}]. \tag{7}$$

The three terms correspond to the reflection amplitude, transmission amplitude, and transmission phase difference, respectively. Herein, we adopt NSGA-II [43], [44], [45], [46] to optimize this multiobjective problem. Unlike single-objective GA that relies on weighted sums to combine objectives, NSGA-II employs a Pareto-based approach. Its mechanisms of fast nondominated sorting, crowding-distance estimation, and elite preservation allow it to efficiently evolve a set of optimal solutions called Pareto front in a single run. From this Pareto-optimal set, the final coding sequence is selected using the ideal-point method. This algorithm enables a superior balance between the amplitude and phase properties of the coupler, which is critical for realizing a high-performance BM within our novel and compact topology.

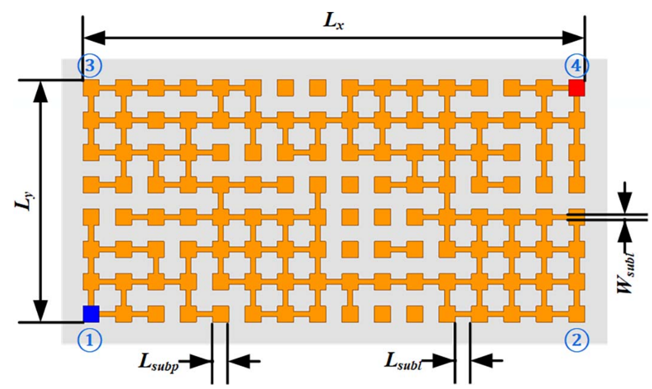

FIG. 4. Structural configurations of the pixel-metamaterial coupler.

For clarity, the target phase differences for the coupler with additional phase shifters in Fig. 3 are listed in the following equations:

$$\varphi_{31} - \varphi_{41} = 90^\circ + \varphi_4 \tag{8}$$

$$\varphi_{42} - \varphi_{32} = 90^\circ - \varphi_4 \tag{9}$$

$$\varphi_{31} - \varphi_{42} = -\varphi_1 + \varphi_4. \tag{10}$$

The detailed structural parameters of the pixel metamaterial are marked in Fig. 4 and summarized in Table I. Each coupler consists of a total of 16 × 8 grid (128 patches) with 232 inner ports. The main ports 1 and 4 that may incorporate additional phase shifters are indicated in blue and red, respectively.

TABLE I. **Structural parameters of the BM (Unit: Millimeters)**

Parameter	Value	Parameter	Value
L_x	9.3	L_{subp}	0.3
L_y	4.5	L_{subl}	0.3
d_0	16	W_{subl}	0.1
d_{gap}	0.8	W_{strip}	0.45

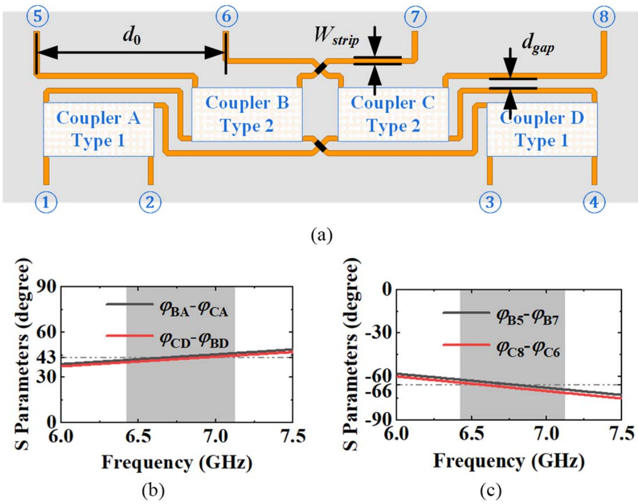

FIG. 5. **(a) Proposed BM with the novel topology. (b) and (c) Phase responses of S_{21} for different transmission-line sections: (b) between coupler A&B/C&D and (c) between coupler B/C and the four output ports.**

All full-wave simulations are performed using the commercial software ansys high frequency structure simulator (HFSS), while the NSGA-II optimizations are executed in MATLAB. In the NSGA-II optimization, the population size is set to 2000, and the maximum number of generations is set to 400. The Pareto fraction and migration fraction are 0.35 and 0.5, respectively. For each pixel coupler, the HFSS pre-simulation with five discrete frequency points takes about 1.5 h, and the subsequent MATLAB-based NSGA-II optimization takes about 3 h on a desktop workstation with an Intel Xeon Platinum 8377C CPU.

BM DESIGN

Coupler Optimization

Based on the topology introduced in the previous section and the phase requirements of the BM, two types of pixel couplers are inserted into the layout, as shown in Fig. 5(a). To facilitate seamless integration with the antenna array, the distance between the two output ports is set to 16 mm, and the line gap is set to 0.8 mm. Notably, the crossover is realized using a simple 0-Ω resistor. The phase delays of different sections of transmission lines are simulated and presented in Fig. 5(b) and (c). From Fig. 2(a), the phase difference between the hybrid couplers (green path minus the black path) is designed to be −45°. However, as observed in Fig. 5(b), the actual difference in this parallel topology is approximately +43°, resulting in a total required compensation of 88°. Leveraging the symmetry

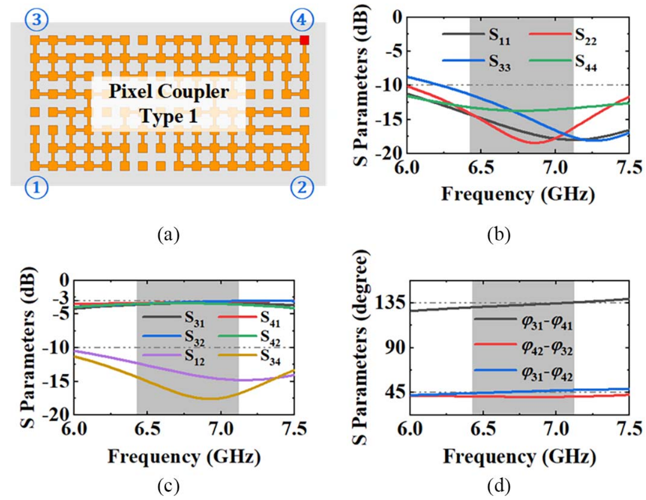

FIG. 6. **Optimized structure and results for the first type of the pixel coupler. (a) Structural details (red patch marks port 4). (b) Reflection coefficients. (c) Magnitudes and (d) phases of transmission coefficients.**

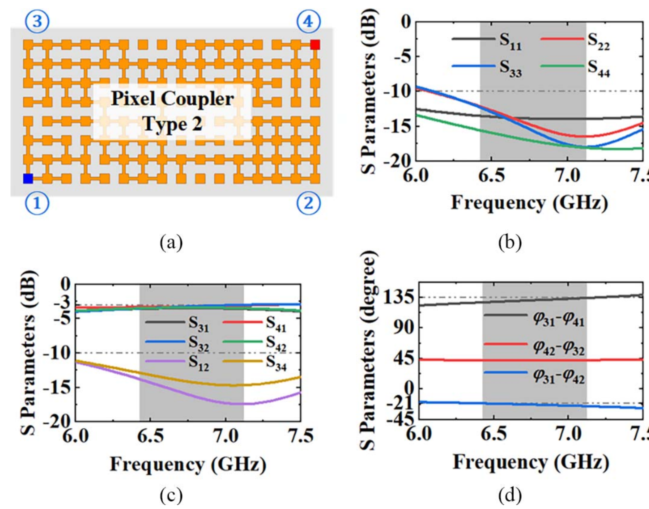

FIG. 7. **Optimized structure and results for the second type of the pixel coupler. (a) Structural details (blue patch marks port 1, and red patch marks port 4). (b) Reflection coefficients. (c) Magnitudes and (d) phases of transmission coefficients.**

of the two couplers, we set the phase shift φ_4 in Fig. 3 for both types to 44°, thereby addressing half of the required compensation. Furthermore, to balance the phase relations between the four output ports of Coupler B/C and the four antenna elements, the phase term φ_1 for type 2 is set to 66°. With these target phase adjustments, the pixel metamaterials for both types of couplers are optimized using the NSGA-II framework. For the first type, the optimized results are presented in Fig. 6. The reflection coefficients and coupling coefficients between any two input ports are all below −10 dB across a broad frequency band, ensuring low reflection and high port isolation. The four transmission amplitudes are close to −3 dB, with an imbalance of less than 1 dB. Critically, as shown in Fig. 6(d), the achieved phase relations are in close agreement with the targets specified in (8)–(10). Similarly, the results for the second type are presented in Fig. 7, where the phase relations also

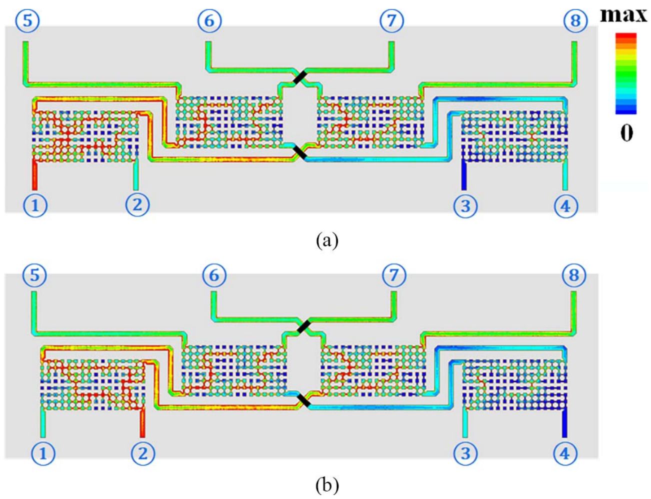

FIG. 8. **Current distributions of the proposed BM when port 1 is excited in (a) and port 2 is excited in (b).**

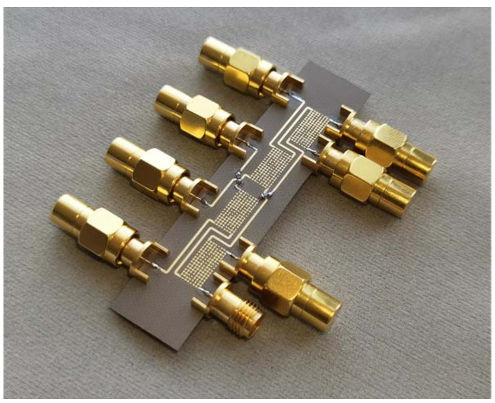

FIG. 9. **Photograph of the prototype of the BM. Seven ports are terminated with 50-Ω absorption loads.**

align with those given in (8)–(10). This consistent agreement for both types of couplers confirms the effectiveness of our design.

Overall Butler Matrix Results

Combining the optimized pixel couplers, we develop the complete BM with an ultracompact size of only 48.5 × 9 mm. The simulated surface current distributions when port 1 or 2 is excited are shown in Fig. 8. Owing to the high degree of optimization freedom provided by pixel metamaterials, it enables more diverse current paths within a constrained area to satisfy the BM's beam-steering requirements. To validate the design, a prototype of the pixel-metamaterial BM is fabricated, as shown in the photograph of Fig. 9. The substrate F4BTM440 is used for fabrication, which is a high-permittivity F4B-based laminate with high-dielectric, low-loss ceramic fillers. Its relative permittivity ε_r is 4.4 and the loss tangent tanδ is 0.0025. Its thickness is only 0.25 mm, making it compatible with integration into the FPC of mobile phones. The BM is fed through eight sub-miniature version A (SMA) connectors. S-parameter measurements are performed using an N9917A vector network analyzer (VNA). For each measurement of a specific S_{mn}, the remaining ports are terminated with 50-Ω absorption loads.

The S-parameter results are all shown in Fig. 10. Across the operating band from 6.3 to 7.4 GHz, which corresponds to a relative bandwidth of 16%, both simulated and measured reflection coefficients are consistently below −10 dB, indicating excellent impedance matching. The port isolations are plotted in Fig. 10(c) and (d), with coupling coefficients of less than −10 dB across the impedance bandwidth. Fig. 10(e)–(h) show the transmission coefficients from the four input ports to the four output ports. Due to port coupling, dielectric loss, and conductor loss, the proposed BM exhibits an average insertion loss of 1.1 dB in simulation and 1.6 dB in measurement. Besides, amplitude and phase imbalance are critical parameters for beamforming networks. The simulation results show that the transmission amplitudes S_{mn} (where n corresponds to ports 1–4 and m to ports 5–8) range from −5.2 to −8.6 dB across the band, resulting in an amplitude imbalance of ±1.7 dB. For measurement, the amplitude imbalance is ±1.6 dB. Regarding phase performance, four clusters of phase differences corresponding to the four input ports are obtained around the target values of ±45° and ±135°. The phase imbalance is ±18° in simulation and ±16° in measurement. These results demonstrate close agreement between the simulation and measurement, confirming the feasibility of the proposed BM. The slight discrepancies are mainly due to fabrication inaccuracies and additional losses. For example, slight variations of the microstrip width may change the characteristic impedance, leading to minor performance degradation in impedance matching.

Discussion

The primary advantage of the proposed BM lies in its ultracompact size and extreme aspect ratio. To quantitatively show the superiority, we conduct a performance comparison between this work and other recently published works on miniaturized BMs in Table II.

Benefiting from the topology design and use of pixel metamaterials, the proposed design has the smallest footprint and the most extreme aspect ratio (defined as length divided by width) among these works. Previous works [18] and [24] achieve excellent beamforming properties such as low amplitude imbalance. However, their lengths and widths are both much larger than one wavelength, rendering them impractical to integrate into mobile phones. Although Jung et al. [22] also reports a small aspect ratio of 0.25, it relies on a multilayer stacked low-temperature co-fired ceramic (LTCC) structure, which increases fabrication complexity, cost, and thickness. In contrast, our design achieves a much wider bandwidth covering the U6G band. Besides, our single-layer substrate fabrication presents distinct low-cost and low-profile advantages over the multilayer folded structure. Compared to [31] with single-objective GA optimization, our design exhibits better beamforming properties with smaller amplitude and phase imbalance, owing to the advanced multiobjective NSGA-II optimization algorithm. This work achieves competitive bandwidth and beamforming performance, with a multifold reduction

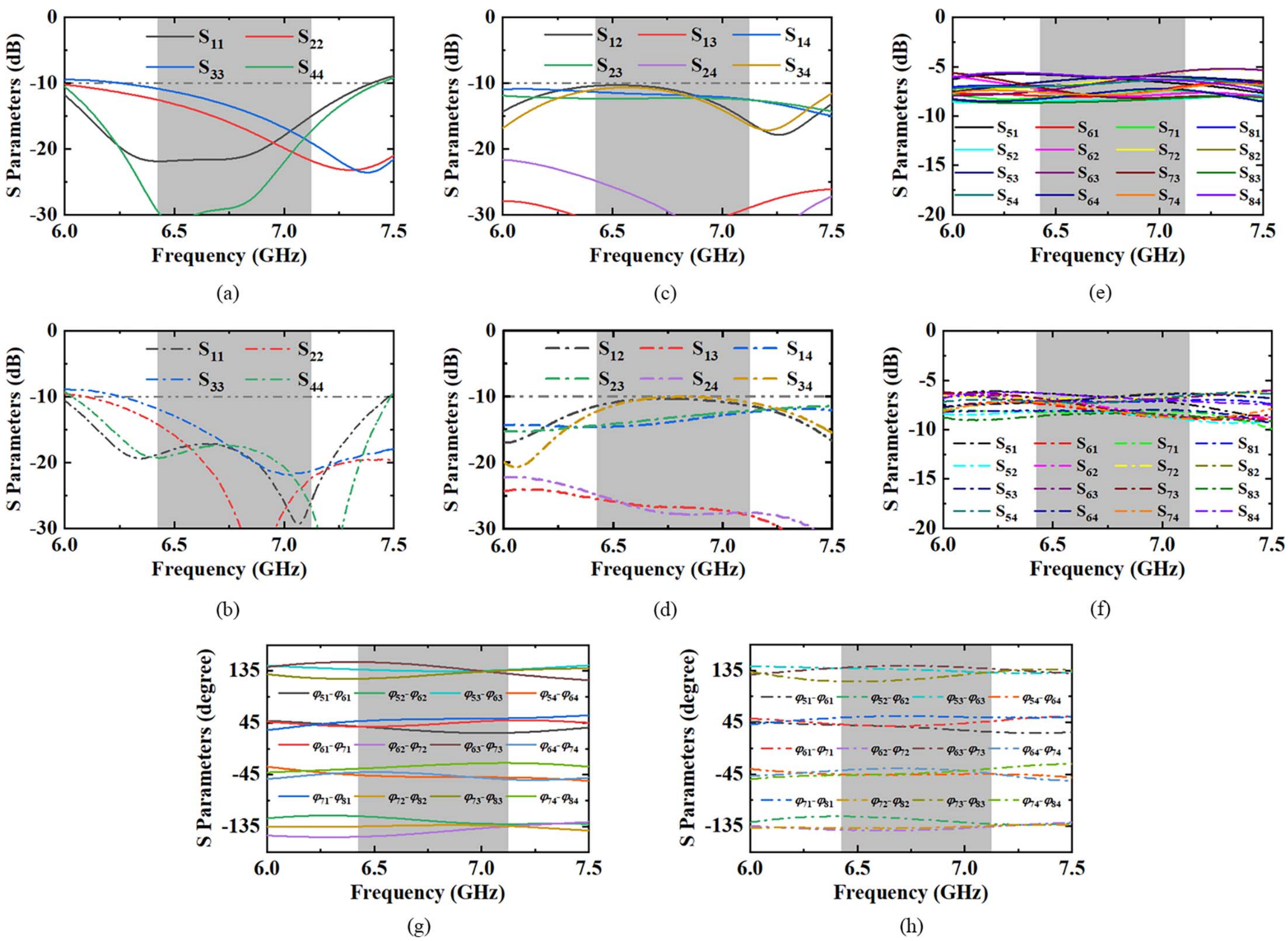

FIG. 10. Results of the proposed pixel-based BM. (a) and (b) Reflection coefficients. (c) and (d) Coupling between each two input ports. (e) and (f) Transmission amplitudes from input ports to outputs. (g) and (h) Transmission phases from input ports to outputs. Solid lines are simulated results, while dashed lines are measured ones.

TABLE II. Performance comparison

Reference	Area (λ^2) (Length × Width)	Bandwidth (%)	Insertion Loss (dB)	Amplitude Imbalance (dB)	Phase Imbalance (degree)	Aspect Ratio
[18]	3.7 × 1.4	6.7	0.6	±1.0	±15	2.64
[22]	0.5 × 2.0	4.7	2.9	±1.2	N. G.	0.25
[24]	2.8 × 1.8	26.0	3.8	±1.1	N. G.	1.56
[31]	1.0 × 0.7	21.6	1.9	±2.2	±25	1.43
This work	**0.2 × 1.1**	**16.0**	**1.6**	**±1.6**	**±16**	**0.18**

Note: N. G.: not given. Bold entries denote the results of our work.

of area, which can better fit the FPC region and leave more space for other circuits, showing its suitability and superiority for space-constrained mobile applications.

For further improvement in the future, structural symmetry and other geometric features can be exploited to reduce the full-wave simulation domain and meshing complexity. Besides, more advanced evolutionary strategies, such as adaptive population size, adaptive crossover/mutation operators, and physics-based constraints on the initial population, can be introduced to accelerate convergence. Deep-learning-assisted surrogate models in [47] may further improve the scalability of the proposed approach for larger BMs.

INTEGRATION WITH ANTENNA ARRAY

To fully validate the performance of the multibeam system in mobile phones, we integrate the proposed BM with a four-element antenna array on the bezel. Dipole antennas are selected because their linear structure is suitable for narrow bezel integration and their broad radiation in the azimuth plane benefits multibeam coverage. Four dipoles are printed on the outer layer of a 1-mm-thick F4B substrate, which is mounted vertically to the mainboard. In addition, the ground plane on the mainboard provides a clearance of 0.3 mm for better radiation. The array is excited by four coupling lines on the FPC, which are connected to the four output ports of the BM.

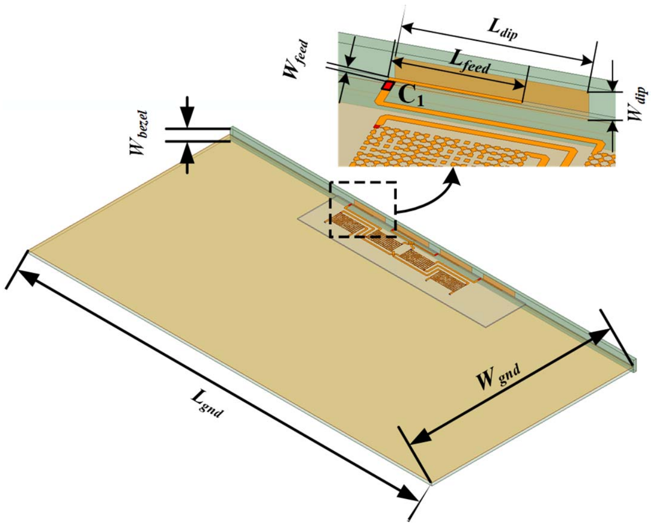

FIG. 11. Structural configurations of the multibeam antenna array deployed on the mobile phone.

TABLE III. Structural parameters of the antenna array (Unit: Millimeters)

Parameter	Value	Parameter	Value
L_{dip}	11.6	L_{gnd}	150
W_{dip}	2	W_{gnd}	75
L_{feed}	8	W_{bezel}	4
W_{feed}	0.3		

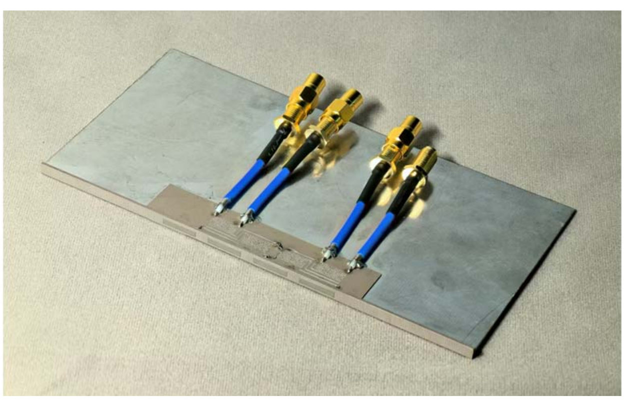

FIG. 12. Photograph of the fabricated multibeam antenna array with four coaxial lines, three of which are connected with absorption loads.

A series capacitor of 2 pF is employed for impedance matching. The detailed parameters of the antenna array are marked in Fig. 11 and summarized in Table III. A photograph of the fully assembled prototype is shown in Fig. 12. S parameters are measured using the VNA, while far-field radiation patterns are measured in an anechoic chamber.

The reflection coefficients are plotted in Fig. 13, showing that the impedance bandwidth covers the entire U6G band. Fig. 14 presents the S-parameters between two input ports, showing isolation levels over 10 dB across most of the U6G band. The minor differences between simulation and measurement results can be attributed to the cable's effects on impedance matching and slight imperfections in the manual assembly process.

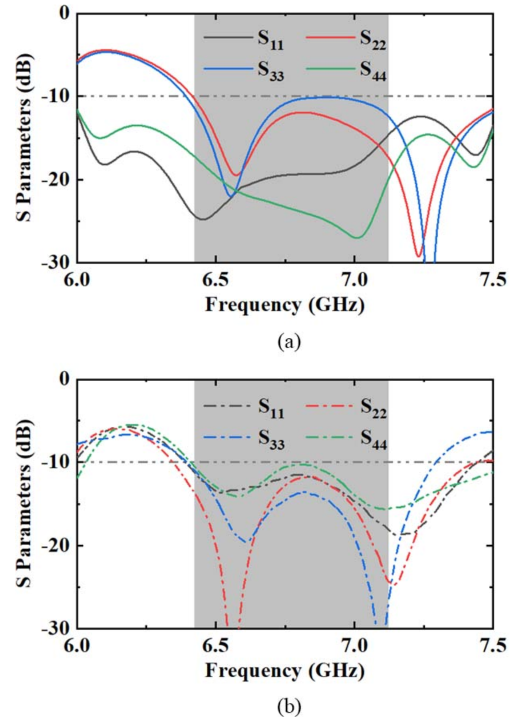

FIG. 13. (a) Simulated and (b) measured results of the reflection coefficients of the multibeam antenna array.

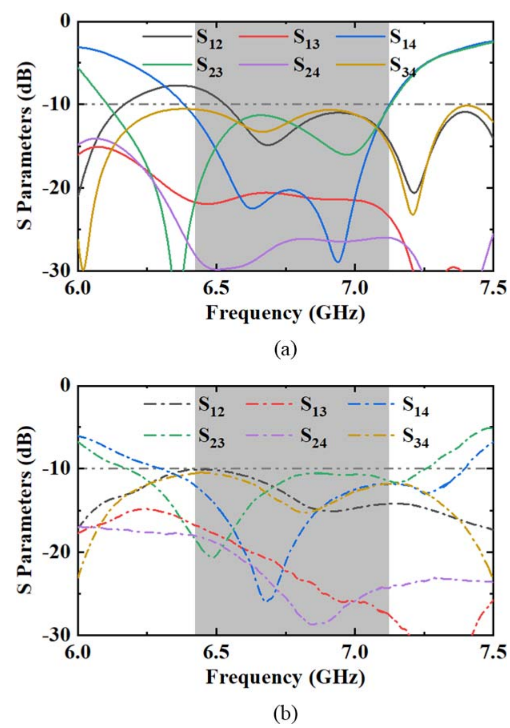

FIG. 14. (a) Simulated and (b) measured results of the coupling coefficients between each pair of input ports of the multibeam antenna array.

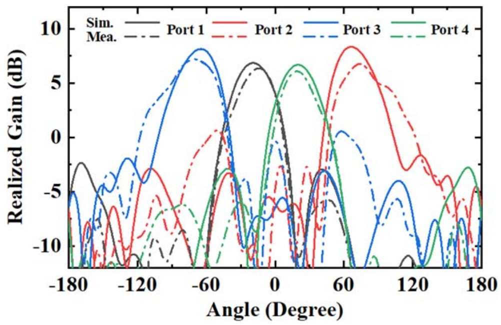

FIG. 15. 2-D radiation patterns for the four steered beams at 6.75 GHz.

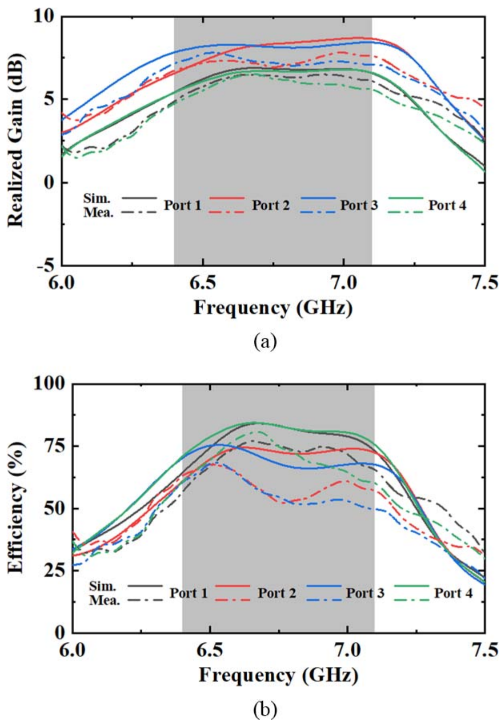

FIG. 16. (a) Peak realized gain; and (b) Total efficiency of the multibeam antenna array.

The 2D radiation patterns for all four ports are measured and shown in Fig. 15. With the BM's beam-steering capabilities, four distinct beams are generated, directed at approximately $\pm 20^{\circ}$ and $\pm 65^{\circ}$, realizing multibeam radiation. Moreover, the main beams cover approximately half of the space, from -90° to 90°, providing superior beam coverage. Simulation verifies that the beam-steering angles are consistent with those of the four-dipole array under ideal excitations, although higher sidelobes are introduced due to the imperfection of the BM. Based on the radiation patterns, the peak realized gains and efficiencies of the four ports are also provided in Fig. 16. Across the whole U6G band, all four beams achieve a peak gain of over 5 dB, compensating for the increased path loss. The total efficiencies of all beams exceed 50%, confirming the system's performance. In summary, by integrating the proposed BM with a bezel antenna array, we further validate the performance of the AI-enabled ultracompact multibeam antenna system for mobile phones.

CONCLUSION

In this article, we propose an AI-enabled pixel-metamaterial BM featuring an ultracompact size and an extreme aspect ratio, making it suitable for deployment in the limited space of mobile phones. A novel topology is introduced to significantly reduce the physical length of the BM, enabling direct integration with a bezel antenna array. The use of pixel metamaterial with NSGA-II optimization framework facilitates this compact layout. As a result, we successfully design a BM with a remarkably small size of only 48.5 mm $\times$ 9 mm $\times$ 0.25 mm, which compresses its length to the subwavelength scale and achieves an extreme aspect ratio of only 0.18. Prototypes of the BM and its integration with a four-element antenna array are fabricated and tested, confirming the feasibility of the proposed approach. The BM operates over a wide bandwidth of 16%, covering the U6G band. When connected to the bezel antennas, the system can generate four beams steered at $\pm 20^{\circ}$ and $\pm 65^{\circ}$, meeting the requirements of reconfigurable radiation patterns for U6G applications. The peak gains exceed 5 dB, and the total efficiencies are over 50% across the U6G band. This work demonstrates a novel and practical beamforming solution enabled by AI-driven optimization, showing significant potential for future U6G communications. Moreover, the methodology of AI-driven metamaterial design is not limited to BM design, but can potentially be extended to other compact microwave components and metamaterial-based devices.

REFERENCES

[1] H. Miao et al., "Sub-6 GHz to mmWave for 5G-advanced and beyond: Channel measurements, characteristics and impact on system performance," *IEEE J. Sel. Areas Commun.*, vol. 41, no. 6, pp. 1945–1960, Jun. 2023.

[2] L. Nan, G. Chunxia, and W. Dapeng, "Considerations on 6 GHz spectrum for 5G-advanced and 6G," *IEEE Commun. Standards Mag.*, vol. 5, no. 3, pp. 5–7, Sep. 2021.

[3] M. J. Emadi, C. Tumula, and S. Hu, "6G coverage enhancement solution using pattern reconfigurable antenna-array at UE," *IEEE Wireless Commun. Lett.*, vol. 14, no. 6, pp. 1763–1766, Jun. 2025.

[4] Z. Jin, J. Tian, Y. Han, X. Li, and S. Jin, "Multi-scenario U6G channel measurement and angular characterization," in *Proc. 16th Int. Conf. Wireless Commun. Signal Process. (WCSP)*, Hefei, China, 2024, pp. 330–335.

[5] T. Liu et al., "Compact U6G massive MIMO antenna arrays with double-layer partial reflective decoupling layers for mutual coupling suppression," *IEEE Open J. Antennas Propag.*, vol. 4, pp. 764–778, 2023.

[6] J. Jiang and L. Zhao, "A compact base station antenna array with high isolation in new U6G frequency band," in *Proc. 14th Int. Symp. Antennas, Propag. EM Theory (ISAPE)*, Hefei, China, 2024, pp. 1–3.

[7] Y. Mo, F. Fan, and X. Zhao, "A compact wide-angle scanning antenna array for U6G massive MIMO Base Station," *2025 IEEE MTT-S Int. Wireless Symp. (IWS)*, Xi'an, China, 2025, pp. 1–3.

[8] Z.-Q. Zhang et al., "Decoupling design of dual-band dual-polarization shared-aperture antenna for 5G and U6G applications," in *Proc. IEEE 10th Int. Symp. Microw., Antenna, Propag. EMC Technologies Wireless Commun. (MAPE)*, Guangzhou, China, 2024, pp. 1–3.

[9] W. Hong et al., "Multibeam antenna technologies for 5G wireless communications," *IEEE Trans. Antennas Propag.*, vol. 65, no. 12, pp. 6231–6249, Dec. 2017.

[10] P. Fu, Y. Zhang, M. Hu, Z. Chen, P. Liu, and Y. Li, "A low-power-consumption massive MIMO scheme based on multibeam antenna array," *Microw. Opt. Technol. Lett.*, vol. 64, no. 8, pp. 1428–1433, Aug. 2022.

[11] Y. Li and K.-M. Luk, “A multibeam end-fire magnetoelectric dipole antenna array for millimeter-wave applications,” *IEEE Trans. Antennas Propag.*, vol. 64, no. 7, pp. 2894–2904, Jul. 2016.
[12] Y. J. Cheng et al., “Substrate integrated waveguide (SIW) Rotman lens and its ka-band multibeam array antenna applications,” *IEEE Trans. Antennas Propag.*, vol. 56, no. 8, pp. 2504–2513, Aug. 2008.
[13] H. Li, Z. Zhou, Y. Zhao, and Y. Li, “Low-loss beam synthesizing network based on Epsilon-near-zero (ENZ) medium for on-chip antenna array,” *Chip*, vol. 2, no. 2, Jun. 2023, Art. no. 100049.
[14] P. Liu, Z. Zhang, Y. Li, and Z. Feng, “A dual-beam eight-element antenna array with compact CPWG crossover structure,” *IEEE Antennas Wireless Propag. Lett.*, vol. 16, pp. 1269–1272, 2017.
[15] J. Butler and R. Lowe, “Beam-forming matrix simplifies design of electronically scanned antennas,” *Electron. Des.*, vol. 9, pp. 170–173, Apr. 1961.
[16] A. K. Vallappil, M. K. A. Rahim, B. A. Khawaja, N. A. Murad, and M. G. Mustapha, “Butler matrix based beamforming networks for phased array antenna systems: A comprehensive review and future directions for 5G applications,” *IEEE Access*, vol. 9, pp. 3970–3987, 2021.
[17] Y. J. Guo, M. Ansari, and N. J. G. Fonseca, “Circuit type multiple beamforming networks for antenna arrays in 5G and 6G terrestrial and non-terrestrial networks,” *IEEE J. Microw.*, vol. 1, no. 3, pp. 704–722, Jul. 2021.
[18] J.-Y. Deng, Y. Zhang, and W. Lin, “Compact multibeam antenna array facilitated by miniaturized slow wave substrate integrated waveguide butler matrix,” *IEEE Trans. Antennas Propag.*, vol. 72, no. 12, pp. 9564–9569, Dec. 2024.
[19] Z. Xu, Y. Shen, S. Xue, and S. Hu, “Miniaturized 4×4 Butler matrix using slow-wave ridged half-mode substrate integrated waveguide,” *IEEE Trans. Circuits Syst. II, Exp. Briefs*, vol. 71, no. 3, pp. 1091–1095, Mar. 2024.
[20] A. A. M. Ali, N. J. G. Fonseca, F. Coccetti, and H. Aubert, “Design and implementation of two-layer compact wideband butler matrices in SIW technology for Ku-Band applications,” *IEEE Trans. Antennas Propag.*, vol. 59, no. 2, pp. 503–512, Feb. 2011.
[21] L.-L. Qiu, L. Zhu, Z.-A. Ouyang, and L. Deng, “Wideband Butler matrix based on dual-layer HMSIW for enhanced miniaturization,” *IEEE Microw. Wireless Compon. Lett.*, vol. 32, no. 1, pp. 25–28, Jan. 2022.
[22] J. Jung, J. Ryu, and K.-Y. Jung, “Multi-beam 5G antenna with miniaturized butler matrix using stacked LTCC,” *IEEE Access*, vol. 11, pp. 125519–125528, 2023.
[23] Y. Zhang and Y. Li, “A dimension-reduction multi-beam antenna scheme with dual integrated butler matrix networks for low-complex massive MIMO systems,” *IEEE Antennas Wireless Propag. Lett.*, vol. 19, no. 11, pp. 1938–1942, Nov. 2020.
[24] L. Van Messem et al., “A 4×4 millimeterwave-frequency butler matrix in grounded co-planar waveguide technology for compact integration with 5G antenna arrays,” *IEEE Trans. Microw. Theory Techn.*, vol. 71, no. 1, pp. 122–134, Jan. 2023.
[25] A. K. Vallappil, M. K. A. Rahim, B. A. Khawaja, and M. N. Iqbal, “A miniaturized metamaterial-loaded switched-beam antenna array system with enhanced bandwidth for 5G applications,” *IEEE Access*, vol. 12, pp. 6684–6697, 2024.
[26] X.-Z. Wang, F.-C. Chen, and Q.-X. Chu, “A compact broadband 4×4 butler matrix with 360° continuous progressive phase shift,” *IEEE Trans. Microw. Theory Techn.*, vol. 71, no. 9, pp. 3906–3914, Sep. 2023.
[27] Y. Zhang, Y. Li, W. Zhang, Z. Zhang, and Z. Feng, “Omnidirectional antenna diversity system for high-speed onboard communications,” *Engineering*, vol. 11, no. 4, pp. 72–79, 2022.
[28] Y. Zhang and Y. Li, “Wideband microstrip antenna in small volume without using fundamental mode,” *Electromag. Sci.*, vol. 1, no. 2, pp. 1–6, Jun. 2023.
[29] S. Wang et al., “Antenna thousandfold miniaturization with ohmic-biased transistor circuit,” *Electromag. Sci.*, vol. 3, no. 2, pp. 0100583-1–0100583-12, Jun. 2025.
[30] S. Tang, Y. Zhang, J. Rao, Z. Han, C.-Y. Chiu, and R. Murch, “Beamforming network design utilizing node microstrip architectures for dual-polarized endfire millimeter-wave antenna arrays,” *IEEE Trans. Antennas Propag.*, vol. 71, no. 6, pp. 4862–4873, Jun. 2023.
[31] P. Fu, Y. Zhang, M. Hu, Z. Zhou, H. Li, and Y. Li, “Subwavelength 8×8 butler matrix with pixel metamaterial for space limited systems,” *IEEE Microw. Wireless Technol. Lett.*, vol. 35, no. 6, pp. 642–645, Jun. 2025.
[32] P. Fu, H. Bu, and Y. Li, “Frequency-multiplexed parallel differentiation in subwavelength planar metastructure,” *Small Struct.*, vol. 6, 2025, Art. no. e2500350.
[33] P. Fu, P. Li, and Y. Li, “Bandwidth enhancement of epsilon-near-zero supercoupling with inverse-designed metamaterials,” *Laser Photon. Rev.*, vol. 19, 2025, Art. no. 2402014.
[34] P. Fu et al., “Reconfigurable metamaterial processing units that solve arbitrary linear calculus equations,” *Nature Commun.*, vol. 15, 2024, Art. no. 6258.
[35] S. Song and R. D. Murch, “An efficient approach for optimizing frequency reconfigurable pixel antennas using genetic algorithms,” *IEEE Trans. Antennas Propag.*, vol. 62, no. 2, pp. 609–620, Feb. 2014.
[36] S. Shen, C.-Y. Chiu, and R. D. Murch, “Multiport pixel rectenna for ambient RF energy harvesting,” *IEEE Trans. Antennas Propag.*, vol. 66, no. 2, pp. 644–656, Feb. 2018.
[37] F. Jiang, C.-Y. Chiu, S. Shen, Q. S. Cheng, and R. Murch, “Pixel antenna optimization using N-port characteristic mode analysis,” *IEEE Trans. Antennas Propag.*, vol. 68, no. 5, pp. 3336–3347, May 2020.
[38] C. Qian, I. Kaminer, and H. Chen, “A guidance to intelligent metamaterials and metamaterials intelligence,” *Nature Commun.*, vol. 16, 2025, Art. no. 1154.
[39] R. L. Haupt, “An introduction to genetic algorithms for electromagnetics,” *IEEE Antennas Propag. Mag.*, vol. 37, no. 2, pp. 7–15, Apr. 1995.
[40] D. S. Weile and E. Michielssen, “Genetic algorithm optimization applied to electromagnetics: a review,” *IEEE Trans. Antennas Propag.*, vol. 45, no. 3, pp. 343–353, Mar. 1997.
[41] J. S. Smith and M. E. Baginski, “Thin-wire antenna design using a novel branching scheme and genetic algorithm optimization,” *IEEE Trans. Antennas Propag.*, vol. 67, no. 5, pp. 2934–2941, May 2019.
[42] N. Nguyen-Trong, L. Hall, and C. Fumeaux, “Transmission-line model of nonuniform leaky-wave antennas,” *IEEE Trans. Antennas Propag.*, vol. 64, no. 3, pp. 883–893, Mar. 2016.
[43] N. Srinivas and K. Deb, “Multiobjective optimization using nondominated sorting in genetic algorithm,” *Evol. Comput.*, vol. 2, no. 3, pp. 221–248, 1995.
[44] K. Deb, A. Pratap, S. Agarwal, and T. Meyarivan, “A fast and elitist multiobjective genetic algorithm: NSGA-II,” *IEEE Trans. Evol. Comput.*, vol. 6, no. 2, pp. 182–197, Apr. 2002.
[45] S. Jayaprakasam, S. K. Abdul Rahim, C. Y. Leow, T. O. Ting, and A. A. Eteng, “Multiobjective beampattern optimization in collaborative beamforming via NSGA-II with selective distance,” *IEEE Trans. Antennas Propag.*, vol. 65, no. 5, pp. 2348–2357, May 2017.
[46] X. Li, W. Dong, L. Wang, Z. Xu, and S. Xiao, “NSGA-II-based hierarchical irregular subarray tiling for large-scale phased array design,” *IEEE Antennas Wireless Propag. Lett.*, vol. 23, no. 10, pp. 3148–3152, Oct. 2024.
[47] Y. Jia, C. Qian, Z. Fan, T. Cai, E.-P. Li, and H. Chen, “A knowledge-inherited learning for intelligent metasurface design and assembly,” *Light-Sci. Appl.*, vol. 12, no. 1, p. 82, Mar. 2023.

Mingzhe Hu (Graduate Student Member, IEEE) received the B.S. degree in electronic engineering in 2022 from Tsinghua University, Beijing, China, where he is currently working toward the Ph.D. degree in electronic engineering.

His research interests include wideband antennas, low-profile antennas, and microstrip antennas.

Mr. Hu serves as a Reviewer for IEEE TRANSACTIONS ON ANTENNAS AND PROPAGATION, IEEE ANTENNAS AND WIRELESS PROPAGATION LETTERS, and *Microwave and Optical Technology Letters*.

Pengyu Fu (Member, IEEE) received the B.S. and Ph.D. degrees in electronic engineering from Tsinghua University, Beijing, China, in 2021 and 2025, respectively.

He is currently a Postdoctoral Fellow with the Department of Electronic Engineering, Tsinghua University. His research interests include metamaterials and metamaterial-inspired antennas.

Dr. Fu serves as a Reviewer for *Microwave and Optical Technology Letters*.

Yongjian Zhang (Member, IEEE) received the B.S. degree in communication engineering from Tongji University, Shanghai, China, in 2018, and the Ph.D. degree in electronic engineering from Tsinghua University, Beijing, China, in 2023.

In 2023, he was a Postdoctoral Fellow with the Department of Electronic Engineering, Tsinghua University. Since 2025, he has been with the Unmanned System Research Institute, Northwestern Polytechnical University, Xi'an, China, where he is currently an Associate Professor. His research interests include phased-array antennas, aircraft antennas, and electromagnetic metamaterials.

Dr. Zhang serves as a Reviewer for IEEE TRANSACTIONS ON ANTENNAS AND PROPAGATION, IEEE ANTENNAS AND WIRELESS PROPAGATION LETTERS, and *Microwave and Optical Technology Letters*.

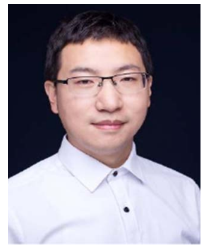

Yue Li (Senior Member, IEEE) received the B.S. degree in telecommunication engineering from Zhejiang University, Hangzhou, Zhejiang, China, in 2007, and the Ph.D. degree in electronic engineering from Tsinghua University, Beijing, China, in 2012.

In 2012, he was a Postdoctoral Fellow with the Department of Electronic Engineering, Tsinghua University. In 2013, he was a Research Scholar with the Department of Electrical and Systems Engineering, University of Pennsylvania, Philadelphia, PA, USA. He was also a Visiting Scholar with the Institute for Infocomm Research (I2R), A*STAR, Singapore, in 2010, and Hawaii Center of Advanced Communication (HCAC), University of Hawaii at Manoa, Honolulu, HI, USA, in 2012. Since 2016, he has been with Tsinghua University, where he is currently an Assistant Professor and an Associate Professor with the Department of Electronic Engineering. He has authored and co-authored over 260 journal articles and 50 international conference papers. He holds 26 granted Chinese patents. His research interests include metamaterials, plasmonics, electromagnetics, nanocircuits, mobile and handset antennas, MIMO and diversity antennas, and millimeter-wave antennas and arrays.

Dr. Li was a recipient of the Issac Koga Gold Medal from URSI General Assembly. He served as an Associate Editor for IEEE TRANSACTIONS ON ANTENNAS AND PROPAGATION and IEEE ANTENNAS AND WIRELESS PROPAGATION LETTERS from 2017 to 2024. He also serves as an Associate Editor for *Microwave and Optical Technology Letters* and *Computer Applications in Engineering Education*.